Supplementary Information (SI) for Journal of Materials Chemistry A.
This journal is © The Royal Society of Chemistry 2024

Supporting information

Experimental Section

Chemicals

Nickel(II) acetate tetrahydrate ($Ni(OAc)_2 \cdot 4H_2O$, 98%, Aldrich), iron(II) sulfate heptahydrate ($FeSO_4 \cdot 7H_2O$, 98%, Aldrich), terephthalic acid (1,4-H_2BDC, Adamas-beta), N,N-dimethylacetamide (DMAC, Greagent), thioacetamide (TAA, Adamas, 99%), ethanol (AR, 99%, Adamas-beta) were used as received. Deionized water was used in all experiments.

Preparation of NiFe-MOF

In a typical synthesis, 0.0496 g of $Ni(OAc)_2 \cdot 4H_2O$ and 0.0166 g of $FeSO_4 \cdot 7H_2O$ were dissolved in 12 mL of DI water followed by adding 12 mL of DMAC solution containing 0.0166 g of 1,4-H_2BDC. The mixture solution was then transferred into a 50 mL Teflon vessel and heated at 150 °C for 3 h. The products were eventually obtained by centrifugation, followed by washing with ethanol and water, and then drying at 60 °C for 3 h. For preparing Ni MOF, the similar synthesis process to that of NiFe-MOF was used expect without adding $FeSO_4 \cdot 7H_2O$.

Preparation of NiFe-MOF-90

Typically, 0.01 g of NiFe-MOF was dispersed in 20 mL of ethanol containing 0.125 g of TAA under stirring for 10 min. Afterwards, the solution was transferred into a stainless-steel autoclave and heated at 90 °C for 3 h. The resulting product (named as NiFe-MOF-90) was collected via centrifugation, washed with ethanol and dried at 60 °C for 3 h. By changing the reaction temperature to 150 °C, the sample of NiFe-MOF-150 was obtained. Following the similar experimental procedure, Ni-MOF could be converted into Ni-MOF-90 and NiS_2 at 90 and 150 °C, respectively.

Characterization

Scanning electron microscopy (SEM) images were acquired by a scanning electron microscope (HITACHI-S4800). Transmission electron microscopy (TEM) and high-resolution transmission electron microscopy (HRTEM) images were collected on Hitachi HT7700 at 120 kV. Chemical composition analyses were obtained using a

JEM-2100F (JEOL, Japan) with an acceleration voltage of 200 kV. XRD patterns were recorded by a Bruker D8 Advanced X-Ray Diffractometer with Cu Kα radiation (λ = 0.154 nm). FTIR spectra were collected on a Nicolet Fourier spectrophotometer using KBr pellets. X-ray photoelectron spectroscopy (XPS) studies were carried out on a Thermo ESCALAB 250 using an Al Kαradiation and C 1s (284.8 eV) as a reference to correct the binding energy.

Electrochemical measurement

Rotating ring-disk electrode (RRDE) tests were carried out using a CHI-760C electrochemical analyzer (CH Instruments Inc.) in a standard three-electrode in O_2-saturated 0.1 M KOH solution at room temperature. A glassy carbon modified with the catalyst, platinum wire and an Ag/AgCl (KCl, 3.5 M) electrode were used as the working, counter and reference electrodes, respectively. The catalyst inks were obtained by dispersing 10 mg of the sample into 1 mL of isopropanol and 40 μL of Nafion solution. The resultant ink was dipped onto the polished glassy carbon disk with a mass loading of 0.61 mg/cm^2 and subsequently dried under an infrared lamp.

The chronoamperometry was performed at 0.5 V vs. reversible hydrogen electrode (RHE) with the ring potential fixed at 1.5 V vs. RHE and RRDE continuously rotated at 1600 rpm. Linear sweep voltammetry (LSV) curves were recorded at a scan rate of 5 mV s^{-1}. A constant voltage of 1.2 V vs. RHE was applied to the ring electrode. The selectivity of H_2O_2 was determined using the following equation:

$$H_2O_2(\%) = \frac{200I_r}{(N \times I_{d+} I_r)},$$

where I_r is the ring current, I_d is the disk current and N is the current collection efficiency of the Pt ring electrode (N=0.258).

To assess the kinetic performance of the catalysts, the Tafel slope (b) was determined by fitting the linear part of the Tafel plots according to the Tafel equation:

$$\eta = a + blog(j) \text{ (a=} \frac{2.303RT}{\alpha nF} \frac{logj_0}{}\text{).}$$

The electrochemical active surface area (ECSA) was calculated based on the double-layer capacitances (C_{dl}) of the catalysts on RDE by cyclic voltammograms (CV) curves

at different scanning rates of 10-100 mV s^{-1} in the non-Faradaic voltage region. A linear relationship can be derived by plotting the current density against the scan rate at a particular potential in cyclic voltammetry curves. The slope of the line is regarded as electrochemical double-layer capacitance (C_{dl}). ECSA can be calculated as:

$$ECSA = \frac{C_{dl}}{A \times Cs},$$

where A is the amount of the material coating on the surface of electrode (mg·cm^{-2}), Cs is an empirical constant representing the capacitance per unit area (40μF·cm^{-2}). Electrochemical impedance spectroscopy (EIS) was measured in 0.1 M KOH solution in the frequency range of 1000 kHz to 0.01 Hz with an amplitude of 10 mV.

The cumulative H_2O_2 yield measurement was conducted in a gas diffusion electrode (GDE) separated by Nafion 117 membrane with Ag/AgCl (KCl, 3.5 M) as the reference electrode, platinum sheet as the counter electrode and the NiFe-MOF-90 modified carbon fiber paper (1 cm×1 cm) as the working electrode. The electrolyzer operated steadily upon increasing the current density from 10 to 90 mA cm^{-2}. The H_2O_2 production rates were calculated by the iodometry method. Typically, 100 μL of reaction solution was collected from the electrochemical system and subsequently added to the mixture of potassium hydrogen phthalate ($C_8H_5KO_4$) and potassium iodide (KI) aqueous solution after reaction for 30 min. The H_2O_2 molecules reacted with I^- to generate I^{3-}(H_2O_2+ $I^- \rightarrow I^{3-}$ +H_2O). The concentration of I^{3-} was measured by a Synergy-H1 microplate reader at its characteristic absorbance peak of 350 nm for H_2O_2 quantification. The stability of catalyst was tested with the chronoamperometric technique at a constant voltage of 0.6 V vs RHE. After continuous stability test, the NiFe-MOF-90 was peeled from conductive glass by ultrasonication in ethanol, then collected by centrifugation, washing with ethanol for 3 times and vacuum dried at 60 ℃ for further characterizations. All the potentials were calibrated with a RHE (E_{RHE}= $E_{Ag/AgCl}$+0.0591×pH+0.197).

Computational details

Spin-polarized density functional theory (DFT) calculations were conducted using the Vienna Ab initio Simulation Package (VASP). The exchange-correlation energy was

treated based on the generalized gradient approximation (GGA) by employing the Perdew-Burke-Ernzerhof (PBE) functional. The electronic energy was regarded as self-consistent when the energy change was smaller than 10^{-6} eV. Geometries were optimized until the energy had converged to 10^{-6} eV/atom and the force converged to 0.05 eV/Å. The structural model of NiFe-MOF-90 and NiS_2 was constructed based on the structure of NiFe-MOF and the NiS_2 cluster. The adsorption energies (E_{ads}) were calculated using the formula $E_{ads} = E_{ad/sub} - E_{ad} - E_{sub}$, where $E_{ad/sub}$, E_{ad} and E_{sub} are the optimized energies of the adsorbate/substrate system, the adsorbate within the structure, and the pure substrate, respectively. The vacuum spacing in a direction perpendicular to the plane of the structure is 18 Å. A 2×2×1 Monkhorst-Pack k-point mesh was used for sampling the Brillouin zone for the relaxation and self-consistency of calculations. To correct the zero-point energy for reaction barrier, the vibrational frequency calculations were performed via the finite-difference approach. All atoms are fully relaxed in the calculations. The free energy was calculated using the equation:

$$G = E + ZPE - TS,$$

where G, E, ZPE and TS are the free energy and total energy from DFT molecular frequency calculations, zero-point energy and entropic contributions, respectively. In our calculation, the top two layers were relaxed, and the other layers were fixed in surface structures.

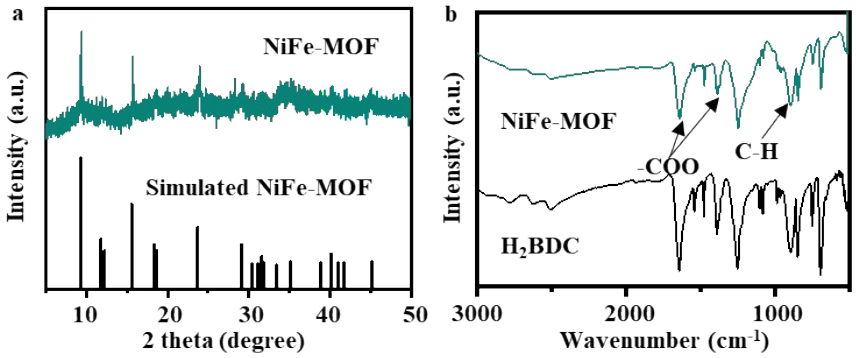

Figure S1. (a) XRD pattern of NiFe-MOF, (b) FTIR spectra of H_2BDC and NiFe-MOF.

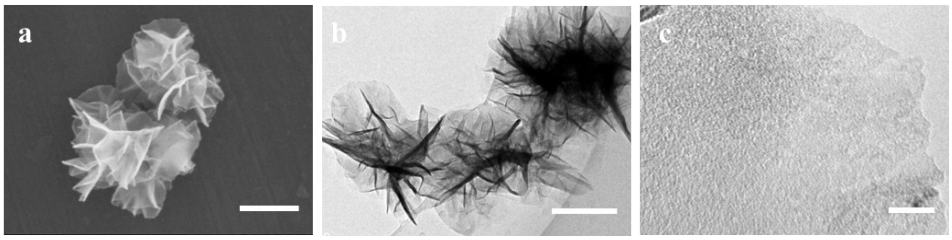

Figure S2. (a) SEM, (b) TEM and (c) HRTEM images of NiFe-MOF. Scale bars are 250 nm (a), 200 nm (b) and 10 nm (c).

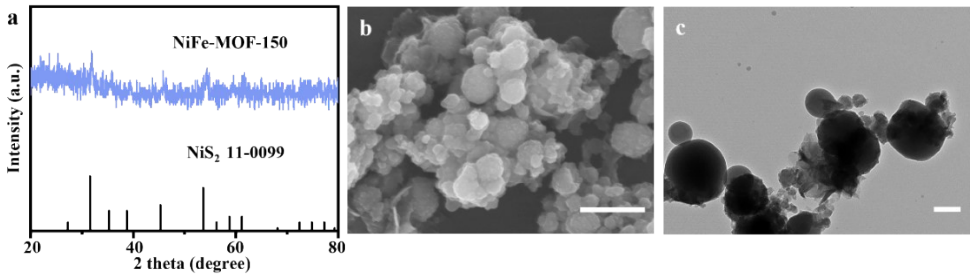

Figure S3. (a) XRD pattern, (b) SEM, (c) TEM images of NiFe-MOF-150. Scale bars are 250 nm (b) and 100 nm (c).

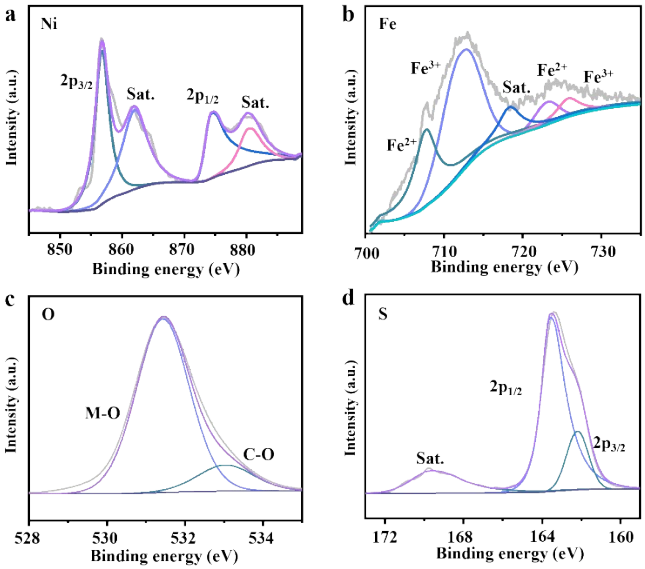

Figure S4. High-resolution XPS spectra of (a) Ni 2p, (b) Fe 2p, (c) O 1s and (d) S 2p of NiFe-MOF-150.

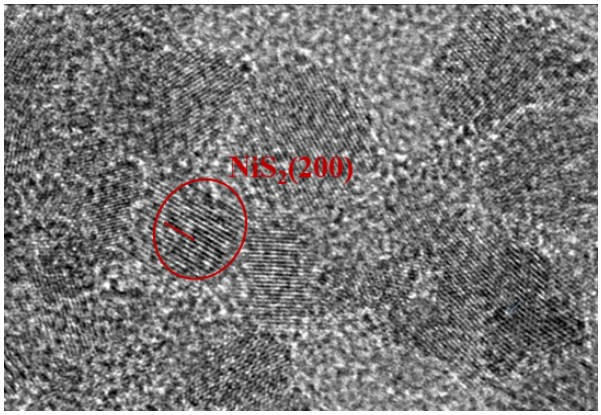

Figure S5. HRTEM images of NiFe-MOF-90 after acid etching.

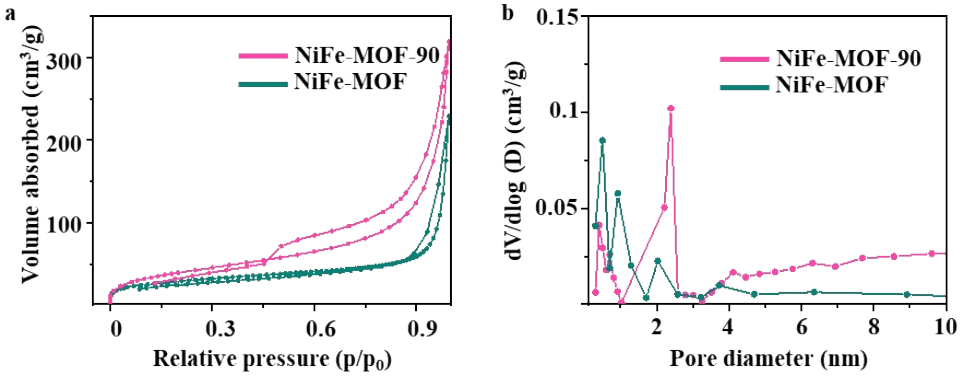

Figure S6. (a) N_2 sorption isotherm, (b) pore size distribution curve of NiFe-MOF and NiFe-MOF-90.

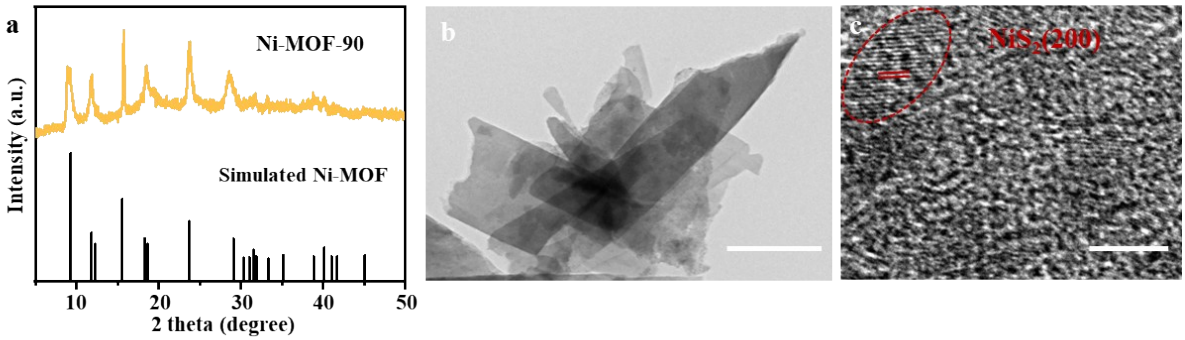

Figure S7. (a) XRD pattern, (b) TEM and (c) HRTEM images of Ni-MOF-90. Scale bars are 1 μm (b) and 5 nm (c).

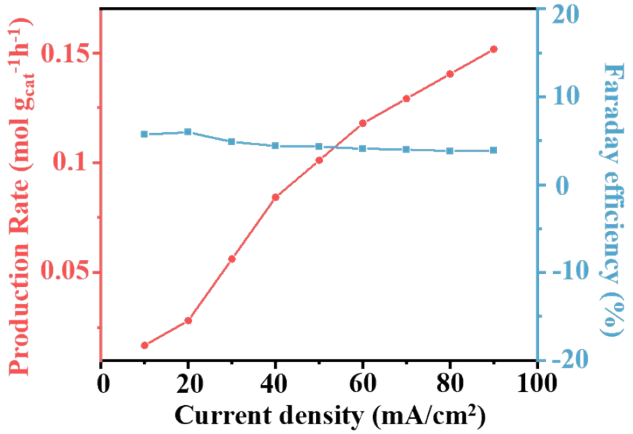

Figure S8. H_2O_2 production rate and Faraday efficiency of pure carbon paper.

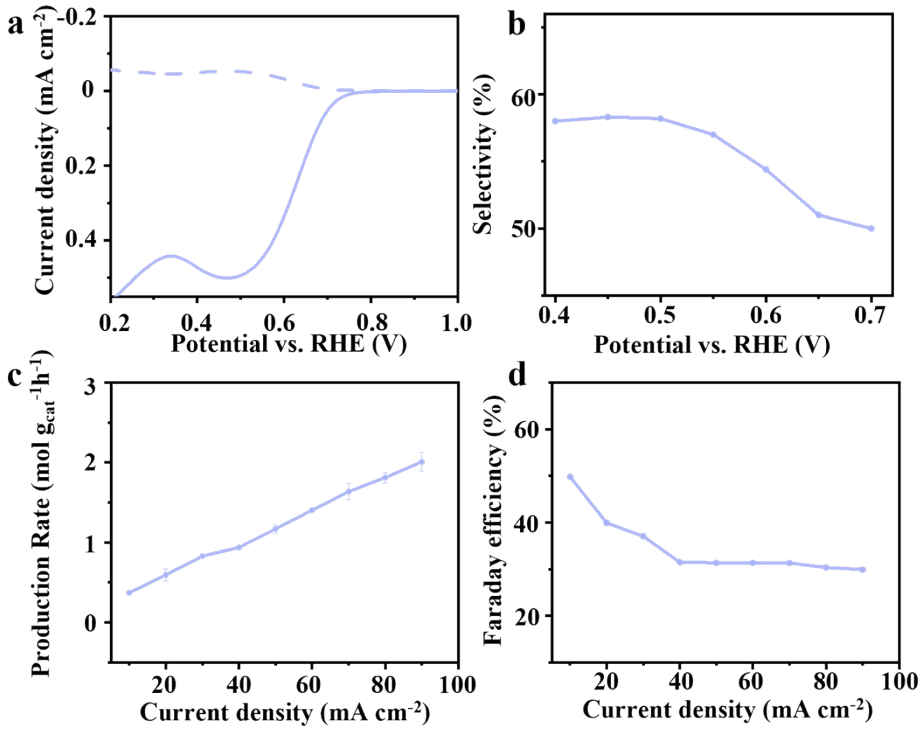

Figure S9. (a) LSV polarization curves, (b) H_2O_2 selectivity, (c) H_2O_2 production rate, (d) Faraday efficiency of NiFe-MOF-150.

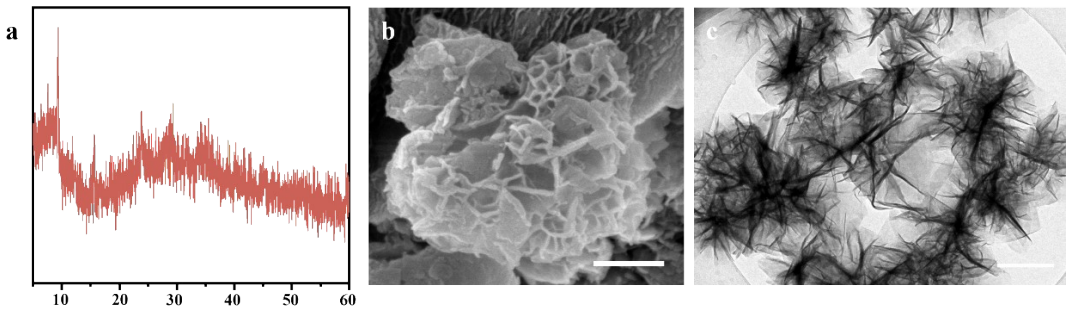

Figure S10. (a) XRD pattern, (b) SEM and (c) TEM images of NiFe-MOF-90 after reaction. Scale bars are 100 nm (b) and 250 nm (c).

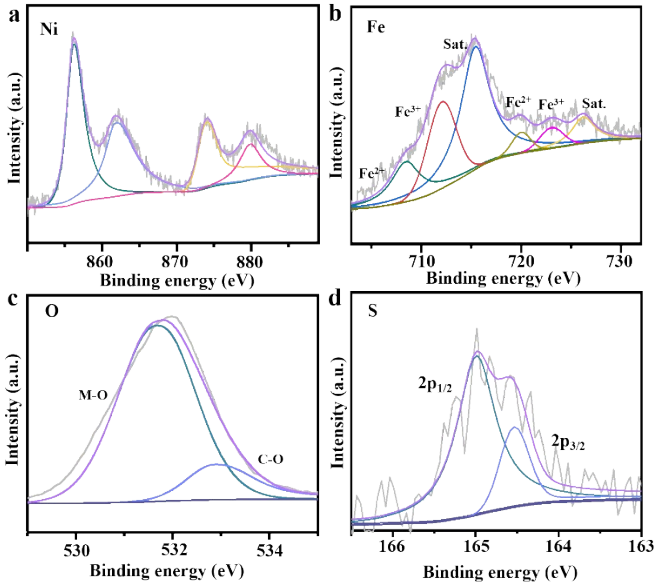

Figure S11. High-resolution XPS spectra of (a) Ni 2p, (b) Fe 2p, (c) O 1s and (d) S 2p of NiFe-MOF-90 after reaction.

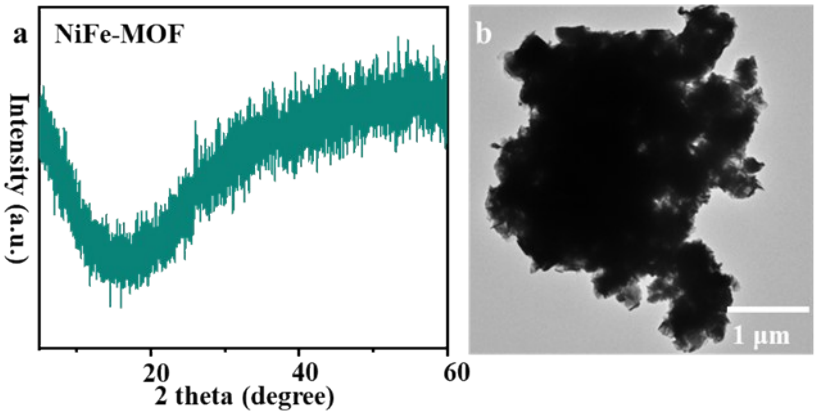

Figure S12. (a) XRD pattern, (b) TEM of NiFe-MOF after reaction. Scale bar is 1 μm.

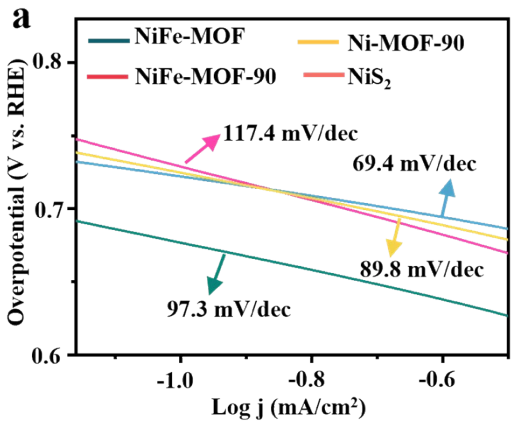

Figure S13. Tafel slope curves of NiFe-MOF, Ni-MOF-90, NiFe-MOF-90 and NiS_2.

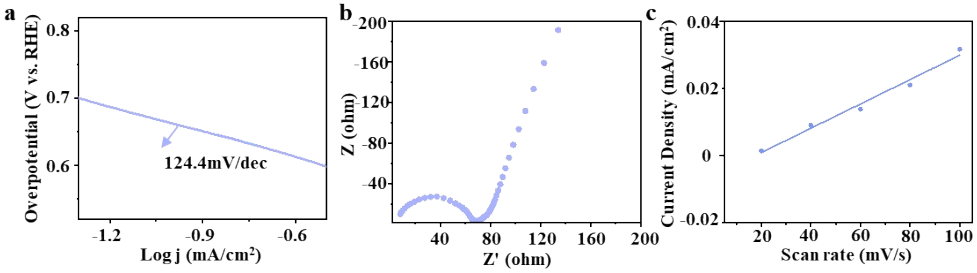

Figure S14. (a) Tafel slope curve. (b) EIS spectrum, (c) CV current density versus scan rate; the linear slope is equivalent to the double-layer capacitance (C_{dl}) of NiFe MOF-150.

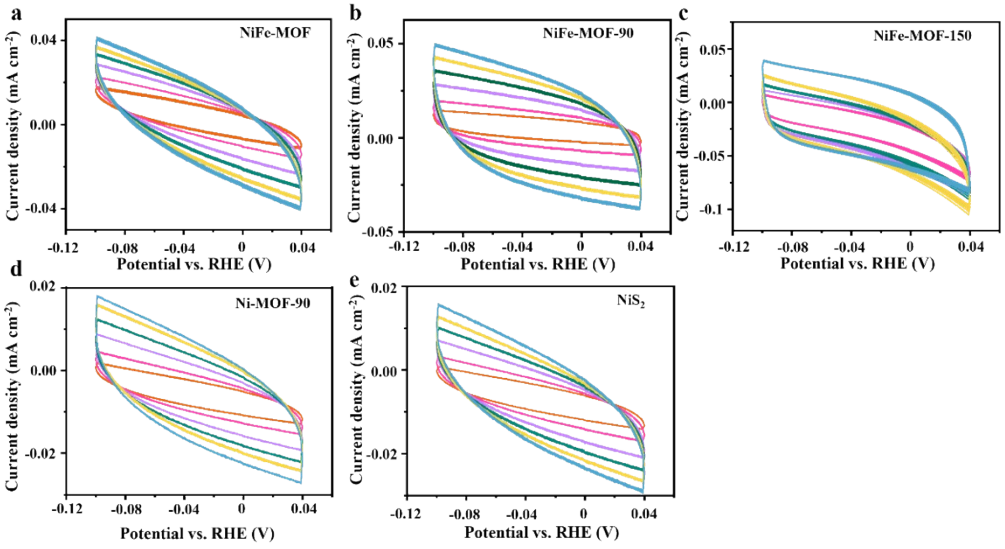

Figure S15. CV curves of NiFe-MOF, NiFe-MOF-90, NiFe-MOF-150, Ni-MOF-90 and NiS_2.

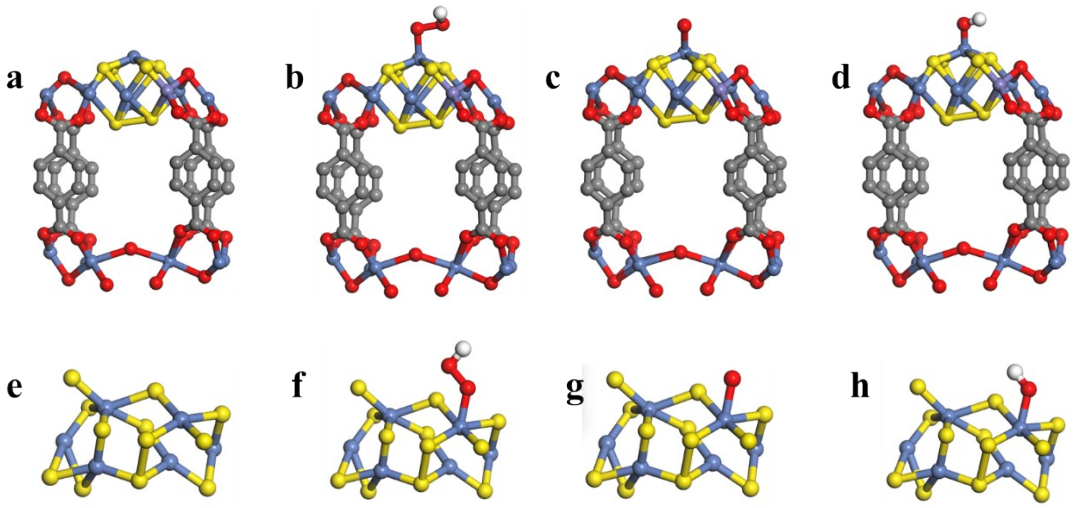

Figure S16. Optimized structures of the reaction intermediates on NiFe-MOF-90 (a-d) and NiS_2 (e-h).

Table S1. ICP results of NiFe-MOF and NiFe-MOF-90 after acid digestion.

Samples	Acid	The ratio of Ni/Fe after digestion
NiFe-MOF	0.1 M HCl	2.80/1
NiFe-MOF-90	0.1 M HCl	2.12/1
NiFe-MOF-90	1 M HCl	2.76/1

Table S2. Comparison of 2e-ORR performance with reported electrocatalysts in alkaline condition.

Catalysts	Electrolyte	Selectivity (%)	H_2O_2 production rate (mol g_{cat}^{-1} h^{-1})	Ref.
C-MOF Ni-250	0.1M KOH	95	0.51	1
Ni MOF NSs	0.1M KOH	98	0.08	2
Cu/Ni-HHTP	0.1M KOH	95	0.793	3
Br-Ni MOF	0.1M KOH	86	0.596	4
Ni_3HAB_2	0.1M PBS	95	0.51	5

ZnCo-ZIF-C_3	0.1M KOH	100	4.35	6
Ti–ZnCoS HSS	0.1M KOH	98	0.675	7
CoS_2	0.05 M H_2SO_4	70		8
α-Fe_2O_3	0.1M KOH	96	0.454	9
O-CNTs	1M KOH	90	0.112	10
CMK3-20	0.1 M KOH	90	2.467	11
Co1–NG(O)	0.1M KOH	80	0.418	12
Co-N-C	0.5 M H_2SO_4	80	4	13
NiFe-MOF-90	0.1M KOH	96	4.2	This work

Table S3. C_{dl} and ECSA values of NiFe-MOF, NiFe-MOF-90, NiFe-MOF-150, Ni-MOF-90 and NiS_2.

Samples	C_{dl} (mF cm^{-2})	ECSA (cm^2 mg^{-1})
NiFe-MOF	0.31	12.7
NiFe-MOF-90	0.25	10.24
NiFe-MOF-150	0.182	7.46
Ni-MOF-90	0.18	7.38
NiS_2	0.15	6.15

Reference

1. H. Wu, T. He, M. Dan, L. Du, N. Li and Z.-Q. Liu, Chem. Eng. J. 2022, 435, 134863.
2. M. Wang, X. Dong, Z. Meng, Z. Hu, Y.-G. Lin, C.-K. Peng, H. Wang, C.-W. Pao, S. Ding, Y. Li, Q. Shao and X. Huang, Angew. Chem., Int. Ed., 2021, 60, 11190-11195.
3. X. Sun, Y. Li, H. Su, X. Zhang, Y. Xu, W. Zhou, M. Liu, W. Cheng and Q. Liu, Appl. Catal. B.. 2022, 317, 121706.
4. M. Liu, Y. Li, Z. Qi, H. Su, W. Cheng, W. Zhou, H. Zhang, X. Sun, X. Zhang, Y. Xu, Y. Jiang, Q. Liu and S. Wei, J. Phys. Chem. Lett, 2021, 12, 8706-8712.
5. R. D. Ross, H. Sheng, Y. Ding, A. N. Janes, D. Feng, J. R. Schmidt, C. U. Segre and S. Jin, J. Am. Chem. Soc, 2022, 144, 15845-15854.
6. C. Zhang, L. Yuan, C. Liu, Z. Li, Y. Zou, X. Zhang, Y. Zhang, Z. Zhang, G. Wei and C. Yu, J. Am. Chem. Soc, 2023, 145, 7791-7799.
7. C. Zhang, R. Lu, C. Liu, J. Lu, Y. Zou, L. Yuan, J. Wang, G. Wang, Y. Zhao and C. Yu, Adv. Sci, 2022, 9, 2104768.
8. H. Sheng, E. D. Hermes, X. Yang, D. Ying, A. N. Janes, W. Li, J. R. Schmidt and S. Jin, ACS Catal, 2019, 9, 8433-8442.
9. R. Gao, L. Pan, Z. Li, C. Shi, Y. Yao, X. Zhang and J.-J. Zou, Adv. Funct. Mater. 2020, 30, 1910539.
10. S. Chen, T. Luo, K. Chen, Y. Lin, J. Fu, K. Liu, C. Cai, Q. Wang, H. Li, X. Li, J. Hu, H. Li, M. Zhu and M. Liu, Angew. Chem., Int. Ed., 2021, 60, 16607-16614.
11. Z. Chen, S. Chen, S. Siahrostami, P. Chakthranont, C. Hahn, D. Nordlund, S. Dimosthenis, J. K. Nørskov, Z. Bao and T. F. Jaramillo, React Chem Eng, 2017, 2, 239-245.
12. E. Jung, H. Shin, B.-H. Lee, V. Efremov, S. Lee, H. S. Lee, J. Kim, W. Hooch Antink, S. Park, K.-S. Lee, S.-P. Cho, J. S. Yoo, Y.-E. Sung and T. Hyeon, Nat. Mater, 2020, 19, 436-442.
13. Y. Sun, L. Silvioli, N. R. Sahraie, W. Ju, J. Li, A. Zitolo, S. Li, A. Bagger, L. Arnarson, X. Wang, T. Moeller, D. Bernsmeier, J. Rossmeisl, F. Jaouen and P. Strasser, J. Am. Chem. Soc, 2019, 141, 12372-12381.